Glaas *et al. Geotherm Energy (2018) 6:14*
https://doi.org/10.1186/s40517-018-0100-9

Geothermal Energy

RESEARCH Open Access

How do the geological and geophysical signatures of permeable fractures in granitic basement evolve after long periods of natural circulation? Insights from the Rittershoffen geothermal wells (France)

C. Glaas[1,2*], A. Genter[1], J. F. Girard[2], P. Patrier[3] and J. Vidal[1]

*Correspondence:
carole.glaas@es.fr
[2] CNRS, UMR 7516 IPGS, University of Strasbourg, 5 Rue René Descartes, 67084 Strasbourg Cedex, France
Full list of author information is available at the end of the article

Abstract

Two deep wells were drilled at Rittershoffen (Alsace, France) to produce high-temperature fluids to supply heat to a biorefinery. The GRT-2 production well was drilled to a depth of 3196 m MD and was deviated to target a permeable local fault in the granitic basement buried beneath a thick sedimentary cover. The objective of this study is to better understand the permeability of fractured reservoirs within crystalline rocks, focusing on the production well GRT-2. Based on a petrographic and mineralogical analysis of cutting samples, several granitic facies associated with hydrothermal alteration were identified on the basis of the amounts of illite, chlorite, anhydrite, secondary geodic quartz, and oxides. These observations were correlated with various geological and geophysical datasets (gamma ray, porosity, density, electrical resistivity, caliper, borehole image logs, temperature, rate of penetration, and mud losses) to localize and identify permeable fracture zones. In sections where acoustic image logs were not available, such as in the deepest part of the well, the geometries of the fracture zones were interpreted from an oriented caliper log. The caliper log interpretation detected one-third of the fractures detected by acoustic image logs. However, two major fracture sets striking N–S and dipping eastward or westward were observed. Furthermore, a synthetic resistivity log that fits the measured resistivity log relatively well was built using the *Archie* and *Waxman and Smits* models. This approach is a proxy for estimating the porosity and the mineralogical changes based on the cation exchange capacity, which is controlled by the chlorite/illite ratio, derived from electrical logs in granitic formations. The correlation of all these results allowed the identification of a resistivity signature of a permeable fracture zone that spatially fits with the temperature signature. The major contribution of this study is the identification of a hierarchy of permeable fractures based on petrophysical signatures. The geophysical signature of fracture zones with low residual permeability exhibits a broad depth extent, whereas the geophysical signature of a highly permeable fracture zone is more localized. Past hydrothermal circulation has enlarged the altered and porous zones around open

fractures, and in some cases, intense illitization has plugged these fracture zones and reduced their permeabilities.

Keywords: Granite, Fracture, Hydrothermal alteration, Mineralogy, Caliper, Resistivity, Geothermal field, Upper Rhine Graben

Background

The economic feasibility of any geothermal project depends mainly on finding the expected resource with a sufficiently high temperature and flow rate to obtain efficient heat production. The sustainability of the geothermal reservoir also needs to be maintained. Geothermal development in Europe and more specifically in the Upper Rhine Graben (URG) has presented a wide range of hydraulic yields from 10^{-3} L/s/bar to 3.5 L/s/bar (Schill et al. 2017; Vidal and Genter 2018). This study aims to investigate preferential channels for natural hydrothermal circulation, their contribution to well permeability, and their history and evolution in terms of secondary mineralogy.

Based on geothermal development in the URG, the permeability of the granitic reservoir appears to be controlled by fractured zones that act as preferential pathways for natural hydrothermal circulation (Dezayes et al. 2010; Ledésert et al. 2010, 1993; Rotstein et al. 2006; Sausse et al. 2010; Sausse and Genter 2005; Vidal and Genter 2018; Villemin and Bergerat 1987). A large number of studies have tried to characterize permeability, fracture geometry, and hydrogeological systems for geothermal applications or nuclear waste storage, whereas a few studies have addressed the hydrogeology of the deep-seated crystalline rocks (Ishibashi et al. 2016; Moreno and Neretnieks 1993; Stober and Bucher 2007). In a volcanic geothermal context, fault zones are also main pathways for fluids (Gailler et al. 2014; Gudmundsson et al. 2002). Fault zones have also been widely studied in outcrops for geothermal applications (Bauer et al. 2015) or at the well or basin scale for oil and gas exploration in sedimentary formations. Deep fracture zones in crystalline rocks have been largely studied with laboratory experiments (Griffiths et al. 2016). However, integrated field examples are lacking (Faulkner et al. 2010). This study proposes field investigations at the well scale, specifically the Rittershoffen GRT-2 production well, in the URG (Fig. 1).

To illustrate how permeable faults are characterized in a geothermal deep-seated granitic reservoir, this study first describes the hydrothermal alterations from mineralogical observations of cutting samples. The structural analysis of fractures with an oriented caliper tool is compared to the structural information from acoustic image logs, and the resistivity response to permeable fault zones and mineralogy is then discussed. Finally, the signature of permeable fractures in the complete well data set is synthesized. This study establishes a hierarchy of fracture zones in terms of permeability based on an original data set from the GRT-2 well.

Rittershoffen geothermal reservoir

The Rittershoffen geothermal site is located in the Upper Rhine Graben in northeastern France, 40 km NNW from Strasbourg and 7 km SE from the well-known Soultz-sous-Forêts geothermal site (Fig. 1). At Rittershoffen, the two deep wells forming the geothermal doublet were designed to supply a biorefinery located close

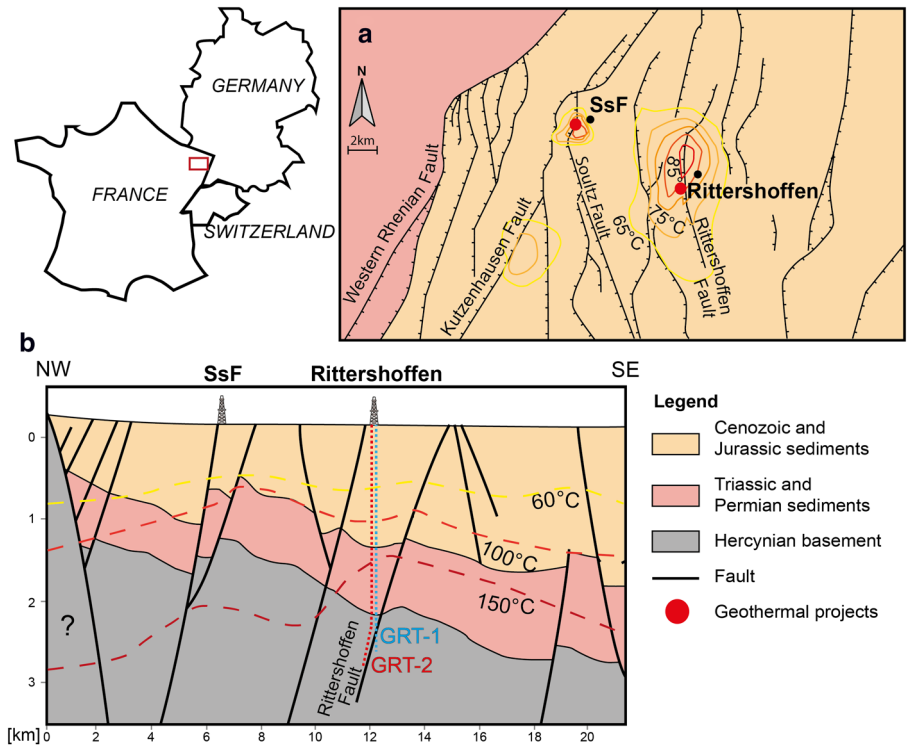

Fig. 1 Location of the Rittershoffen geothermal site. **a** Simplified geological and structural map of the Rittershoffen and Soultz-sous-Forêts (SsF) area. The isotherms at the top of the basement are from Baillieux et al. (2014). **b** Geological cross section through the Rittershoffen and Soultz-sous-Forêts geothermal sites with the Rittershoffen well trajectories, after the GeOrg Team (2017). The dashed lines are schematic trajectories of the GRT-1 (blue) and GRT-2 (red) geothermal wells (Vidal et al. 2018)

to the Rhine river and to produce 24 MWth (Baujard et al. 2017a). Via a downhole pump, the GRT-2 production well produces a geothermal brine at industrial rates of 70 L/s, with water temperatures of up to 168 °C at the surface and a salinity close to 100 g/L (Sanjuan et al. 2016). In the Upper Rhine Graben, natural flow rates are low and can be enhanced by thermo-hydro-mechanical-chemical (THMC) stimulation, such as that used in the Soultz wells or at Rittershoffen in the GRT-1 well (Baujard et al. 2017a; Schill et al. 2017). The objective of the enhanced geothermal system (EGS) technology is to improve the connectivity between the well and the reservoir and thus the well productivity. In contrast, the GRT-2 production well is one of the most permeable wells in northern Alsace and is not stimulated after drilling operations, because its natural productivity index was sufficiently high (Baujard et al. 2017a; Vidal and Genter 2018). The geothermal reservoir is located at the interface between the sedimentary cover and the crystalline basement. At the interface, the sedimentary cover comprises Triassic sandstones. The crystalline granitic basement is composed of muscovite, biotite, *K*-feldspar, plagioclase, and quartz, and is interpreted to be equivalent to the two-mica granite encountered in the deep reservoir at Soultz (Stussi et al. 2002; Traineau et al. 1992). The formation of the granitic basement has been dated to the mid-Carboniferous, and it has since undergone pervasive alteration and exhibits several grades of hydrothermal alteration (Cocherie et al.

2004; Genter 1989). In the granite, the GRT-2 well productivity is supported by four main permeable fracture zones (Baujard et al. 2017a). They were detected in the temperature log at 2533 m measured depth (MD), from 2770 to 2808 m MD, from 2940 to 2980 m MD, and from 3050 to 3072 m MD (Fig. 2). These zones are strongly supported by the mud loss data, which are correlated with the temperature anomalies. The mud losses increase by approximately 3 m^3/h at 2530 m MD, approximately 3 m^3/h at 2795 m MD, approximately 2 m^3/h at 2810 m MD, and approximately 5 m^3/h at 2985 m MD (Fig. 2). In addition, this permeability evidence at the well scale is systematically correlated with increases in the rate of penetration (ROP) at depths of 2535, 2770, 2787, 2800, 2948, and 3050 m MD.

Borehole data and methods

Datasets

This study focuses on the open-hole sections of the Rittershoffen wells in the granitic basement and more precisely on the GRT-2 production well, which intersects many permeable fractures. The following table (Table 1) presents the available data acquired in the open-hole granitic sections of wells GRT-1 and GRT-2 (Figs. 2, 3, 5). The open-hole sections in the granite parts of both wells have lengths of 365 m for GRT-1 and 716 m

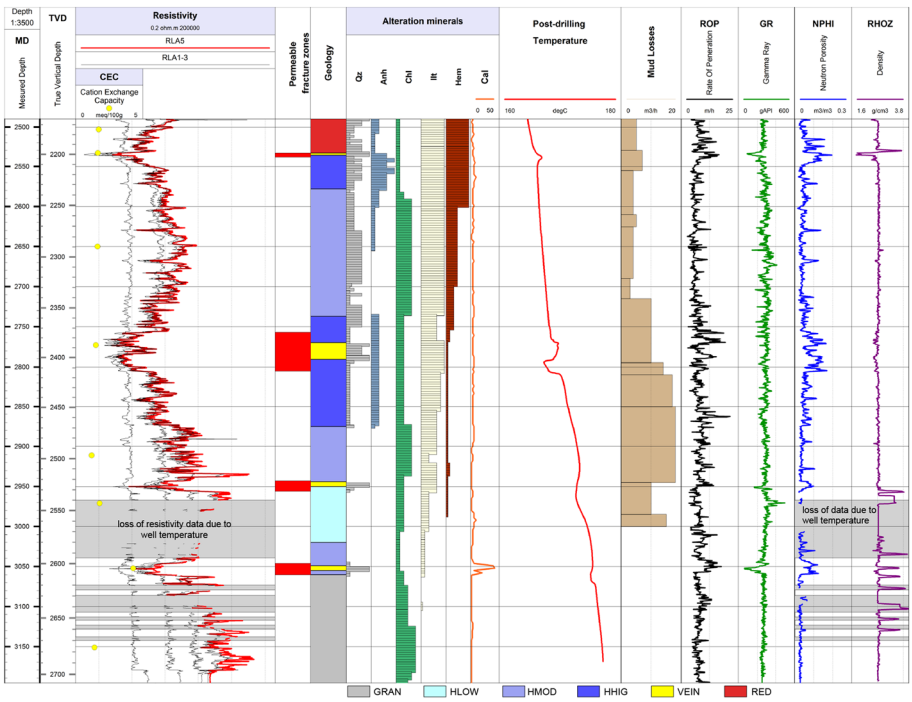

Fig. 2 Composite log of the GRT-2 granitic basement, including alteration mineral quantities from cutting observations and the following geophysical logs: resistivity, temperature, mud losses, rate of penetration (ROP), gamma ray, porosity, and density. The permeable fracture zones (in red) were deduced from the complete data set presented here and were based on the previous studies (Vidal et al. 2017). The gray areas represent loss of data due to well temperatures that were too high. The facies are as follows: GRAN: granite, HLOW: low hydrothermal alteration grade, HMOD: moderate alteration grade, HHIG: high alteration grade, VEIN: quartz vein, RED: reddish granite

Table 1 Details of the geological and geophysical data sets available for the granitic basement of the GRT-1 and GRT-2 wells

	Name	Depth (MD) GRT-1	Depth (MD) GRT-2	Unit	Vertical resolution–*Horizontal resolution*
Mud logs	Cuttings	2215–2580 m, 122 samples	2480–3196 m, 239 samples	No unit	Sampled each 3 m in-depth
	CEC	No CEC measurements in GRT-1	2503–3151 m, 8 samples	meq/100 g	CEC measurements were performed on crushed cutting samples
	Calcite	2215–2580 m	2480–3196 m	m^3/m^3 (expressed in %)	Calcimeter measurements were performed on crushed cutting samples
	Mud losses	2215–2580 m	2480–3196 m	m^3/h	Driller observations
	Rate of penetration (ROP)	2215–2580 m	2480–3196 m	m/h	50 cm
Geophysical logs	Gamma ray (GR)	2215–2570 m	2480–3196 m	gAPI	15 cm
	Hole diameter	2215–2580 m	2480–3008 m	Inches	15 cm *60°*
	BoreHole image	2480–2865 m	2480–2865 m		1 cm *2°*
	Resistivity	No resistivity log in GRT-1	2480–3196 m	ohm m	15 cm
	Porosity	2215–2577 m	2480–3196 m	m^3/m^3	15 cm *depth of investigation: several cm (flushed zone)*
	Density	2215–2580 m	2480–3196 m	g/cm	15 cm
	Temperature	2215–2470 m	2480–3169 m	°C	GRT-1 = 20 cm GRT-2 = 50 cm

The first column presents the type of data; columns two and three present the measured depth intervals in the two open-hole sections. The fourth column presents the units of the data, and the fifth column presents the resolution of the data according to the log acquisition resolution, both vertically and horizontally (in italic letters)

for GRT-2. Mud logs were acquired during drilling operations and have a spatial resolution between 20 and 50 cm, whereas the geophysical logs were acquired after drilling and have a vertical spatial resolution of approximately 15 cm. The cutting samples were collected at depth intervals of every 3 m during drilling. Because one sample represents 100 L of rock (Table 1), the vertical resolution of cutting is thus quite coarse and is not as precise as core samples; in addition, cutting samples provide no information on the rock texture (Fig. 4).

Secondary mineralogy from cuttings

The petrographic logs in the open-hole sections of both wells are based on cutting observations with a binocular magnifier. In the GRT-2 well, 240 cutting samples collected in the basement were thoroughly observed and investigated in terms of primary and secondary mineralogy. According to the previous studies on the Soultz-sous-Forêts geothermal site, the hydrothermal alteration grades in the granite are well known from core observations (Ledésert et al. 1999; Meller et al. 2014; Meller and Kohl 2014; Meller and Ledésert 2017; Sausse et al. 2006; Traineau et al. 1992). The

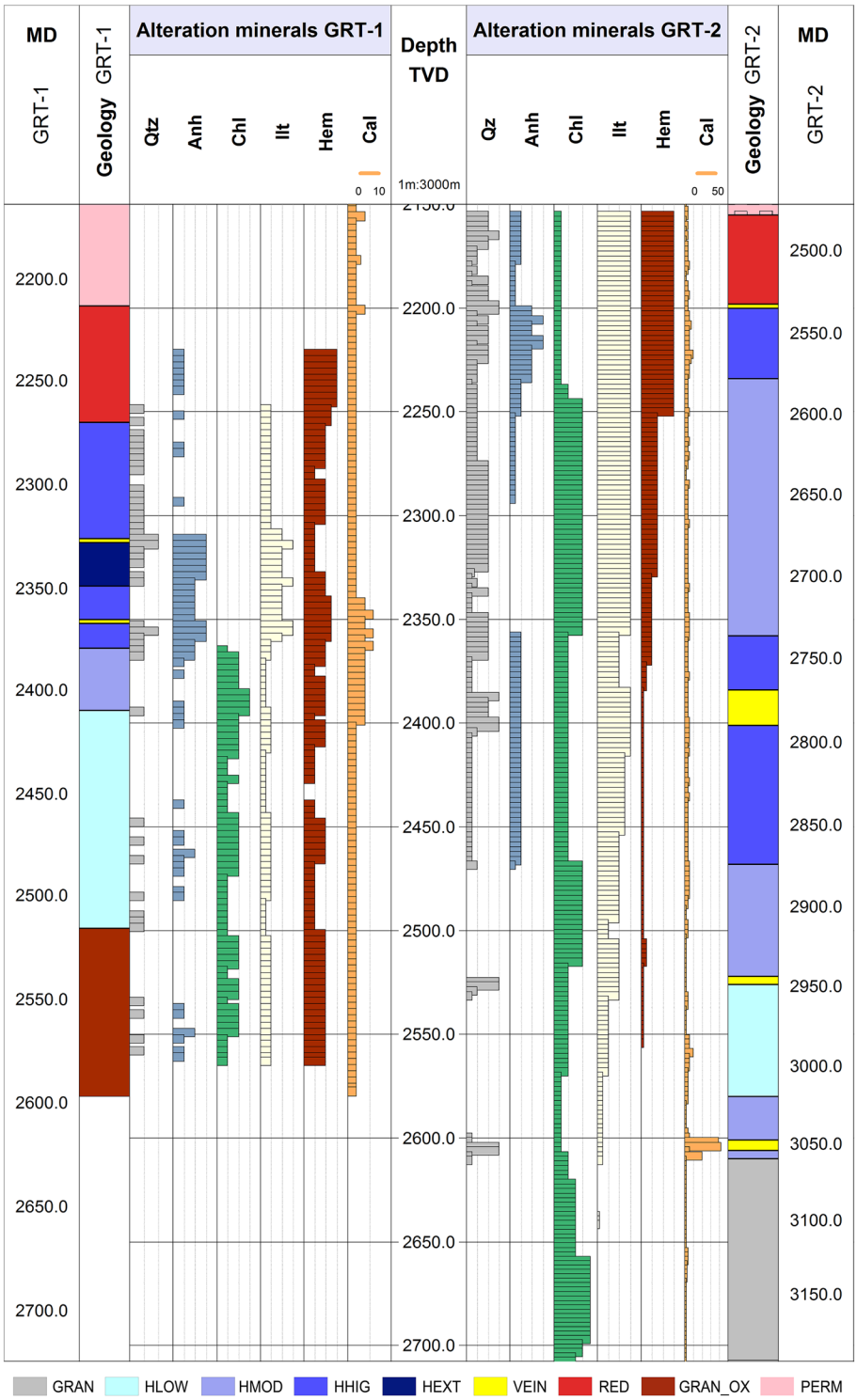

Fig. 3 Geological logs of both the GRT-1 and GRT-2 wells, based on the mineralogical quantities observed in cuttings. The reference depth is TVD for both wells. The facies are as follows: GRAN: granite, HLOW: low hydrothermal alteration grade, HMOD: moderate alteration grade, HHIG: high alteration grade, HEXT: extreme hydrothermal alteration, VEIN: quartz vein, GRAN_OX: oxidized granite, RED: reddish granite, PERM: Permian sandstone

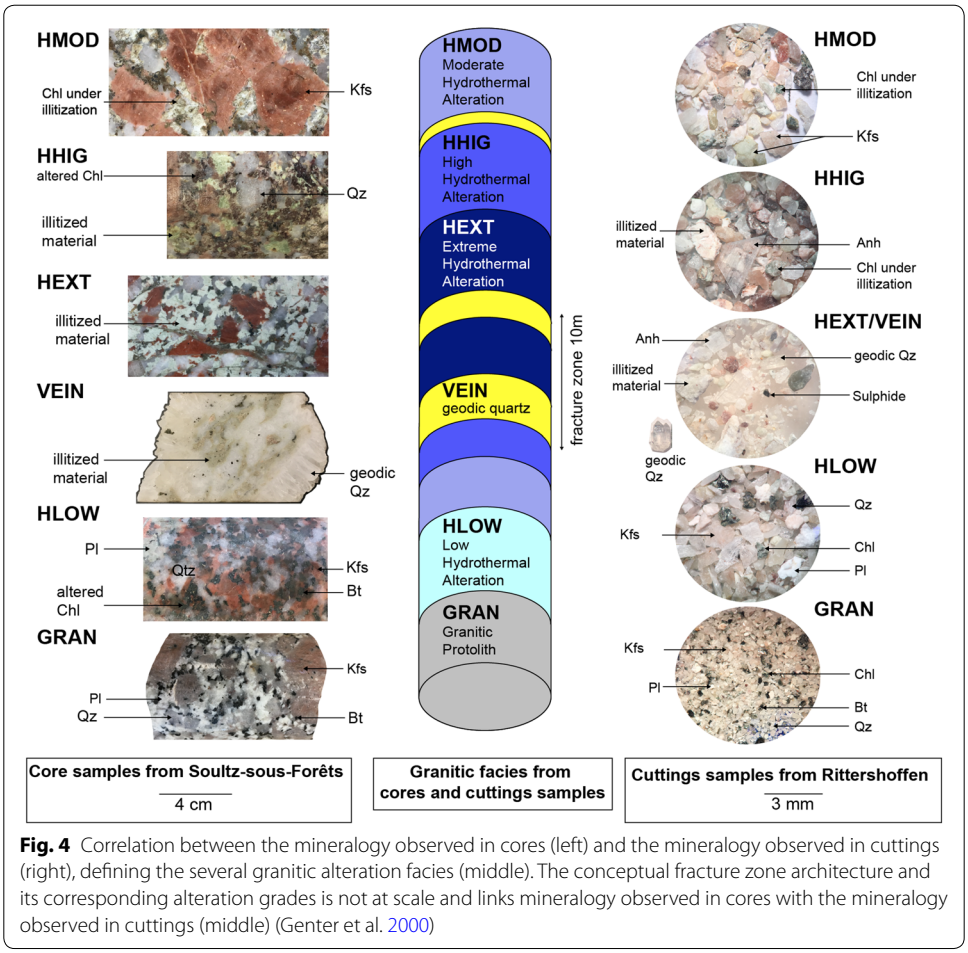

Fig. 4 Correlation between the mineralogy observed in cores (left) and the mineralogy observed in cuttings (right), defining the several granitic alteration facies (middle). The conceptual fracture zone architecture and its corresponding alteration grades is not at scale and links mineralogy observed in cores with the mineralogy observed in cuttings (middle) (Genter et al. 2000)

core mineralogy and hydrothermal alteration grades were cross-referenced with the minerals observed in the cuttings, although the texture information and the mineral assemblage were not reflected in the cuttings (Fig. 4). In the cutting samples, several hydrothermal alterations and granite facies were distinguished. The mineralogy was described through a semi-quantitative approach using a three-class scale. The low hydrothermal alteration (HLOW) grade is characterized by more chlorite than primary biotite, the absence or small amount of illite, and intact plagioclase (feldspars). The moderate hydrothermal alteration (HMOD) grade is characterized by the presence of illite due to further alteration of the chlorite and intact feldspars. The high hydrothermal alteration (HHIG) grade is associated with abundant illitic material, very low amounts of chlorite, and altered plagioclase. The extreme hydrothermal alteration (HEXT) grade is characterized by abundant illitic material from biotite and plagioclase transformation and geodic quartz prisms linked to hydrothermal circulation (Genter et al. 1997; Traineau et al. 1992). The VEIN facies defines the fracture zones identified by the highest amounts of secondary geodic quartz precipitation and is associated with a high calcite content (Hébert et al. 2010). The granitic facies identified in the cuttings include unaltered granite (GRAN), which is characterized by the presence of biotite, hematite, and calcite, and is associated with a propylitic

alteration related to the emplacement of the pluton (Genter et al. 2000; Jacquemont 2002), and reddish granite (RED), which contains a large amount of red *K*-feldspar megacrysts oxidized through intense exposure to weathering fluids. The oxidized granite (GRAN_OX) in GRT-1 is a propylitic granite that also presents a pronounced reddish color associated with oxidation and a large amount of hematite.

The presence of illite in the granitic basement and as a major signature of hydrothermal alteration was also confirmed by complementary analyses. In the previous studies, X-ray diffraction (XRD) was performed on the clay fraction (< 5 μm) of selected cuttings, from which three groups of illitic minerals (well-crystallized illite, poorly crystallized illite, and illite-rich illite/smectite mixed layers) were identified (Vidal et al. 2018). The chemical compositions of the clay minerals (illite and chlorite) were obtained using a scanning electron microscope (SEM) coupled with energy-dispersive X-ray spectroscopy (EDS). This study showed that permeable fractured zones were associated with the occurrence of poorly crystallized illite and illite/smectite mixed layers crystallized during hydrothermal circulation. In the GRT-2 well, some Fe-chlorite was also observed in highly permeable fracture zones that were not totally plugged by small crystallites of illite (Vidal et al. 2018).

The cation exchange capacity (CEC) value is the number of negative sites that can store cations such as K, Ca, Mg, Na, and H+. This index provides information about the amount of swelling clays that the rock contains, as the types of clays are known from XRD analyses. CEC analyses were performed on selected cutting samples from the GRT-2 well to quantify the amount of swelling clays (Fig. 2). The measurement was performed on crushed cuttings with the standard cobaltihexamine chloride method NF X31–130 (1999). Calcimetry was performed on samples from both wells during the drilling and provided information about the relative amount of calcite, dolomite, or total carbonates in the cutting samples (Fig. 3). More precisely, the use of a calcimeter on the crushed and dried cuttings measures the quantity of CO_2 released by the reaction of the carbonates with HCl. The quantity of CO_2 released after 1 min gives the percentage of calcite, and the quantity of CO_2 released after 15 min gives the percentage of total carbonates. The difference between the total carbonate quantity and the calcite quantity is the amount of dolomite. The two superimposed curves reveal that only calcite is present in the granitic sections of the GRT-1 and GRT-2 wells.

Mud logging

Mud logs are instantaneous well logs, and include data on mud losses, gas content, ROP, and many standard drilling parameters. They are the first indicators of the occurrence of permeable zones in a well. In fact, they are acquired during drilling before the other logs. Mud losses provide information on the quantity of mud that is lost through a permeable fractured zone in the well, and they are recorded by the driller and are thus approximations of the fracture zone permeability. The ROP, which provides information on rock softness, has an average value of 3 m/h in the massive granitic Soultz basement, indicating a hard granite; values higher than 5 m/h indicate that the granite is fractured and/or altered (Fig. 2) (Baujard et al. 2017b). In the GRT-2 borehole, especially in the granitic basement, the ROP is very high, with values of approximately 9–10 m/h, due to the hydrothermal alteration that makes the granite easier to drill (Baujard et al. 2017b).

Structural analysis from caliper data

The acoustic image log (UBI) (Fig. 5b) enables the identification of natural and induced fractures as well as their geometries and the determination of the in situ principal horizontal stress orientation. In both wells, GRT-1 and GRT-2, the structural information on natural fractures was derived from the acoustic image log (Vidal et al. 2017). The dip, dip direction, and fracture density were calculated. The GRT-2 well is inclined and crosscuts many fractures, with large cave zones in its deepest part. Stick–slip processes occurred, leading to poor data quality in some zones and the complete absence of data acquisition in the deepest part of the well between 2800 and 3196 m MD (2409–2707 m MD) in the worst case (Vidal et al. 2017). In this study, an additional structural information was derived from the caliper log, which was associated with an orientation system (Fig. 5a), to complete the structural dataset. A new method was then developed for locating, measuring and orienting the geometry of first-order natural fractures based on a standard tool. The caliper tool measures 6 radii that are spaced approximately 60° from each other in the borehole (Fig. 5a). In an inclined well like GRT-2, the caliper data must be corrected; in fact, the measured radii are skewed, because the center of the tool is not centered in the borehole. Due to this sampling bias, the radii corresponding to the lower portion of the borehole wall are shorter, and the radii corresponding to the upper portion of the borehole wall are longer. This discrepancy causes enlargements in radii that are due to the sampling bias rather than to natural fractures. Moreover, the tool rotates during the acquisition, and therefore, radius measurements also need to be reoriented. Therefore, calculations and corrections such as centering and data orientation were applied to the caliper data to identify enlargements in the radius due to natural fracture occurrences in the caliper radii curves. More precisely, the centering process was performed by geometrically shifting the caliper tool center to the center of the borehole, and then, the caliper arm lengths were recalculated, thereby avoiding the effects of gravity in an inclined borehole. In addition, the azimuthal positions of the measured radii were calculated using the azimuthal position of the first arm followed by extrapolation to the other arms, as the arms are spaced by approximately 60°. This calculation was performed to avoid artifacts resulting from rotation of the tool in the borehole during data acquisition and enabled plotting of the oriented caliper data with depth to be able to calculate the fracture dip and dip direction.

Then, fractures were picked on the corrected caliper log to calculate their dip and dip directions (Fig. 5). Radius anomalies visible in the six non-oriented curves (Fig. 5a, left) were identified and then placed at the same depth on the oriented caliper log (Fig. 5a, right) to fit a sinusoid that represents the fracture based on several identified radius anomalies.

Geophysical logs

Once a permeable zone was detected in the mud logs, the geophysical logs' responses corresponding to that zone were also studied (Fig. 2). The geophysical logs enabled the identification of open permeable fractures at the borehole scale and in the best cases assisted in characterizing the flow contribution of the fracture.

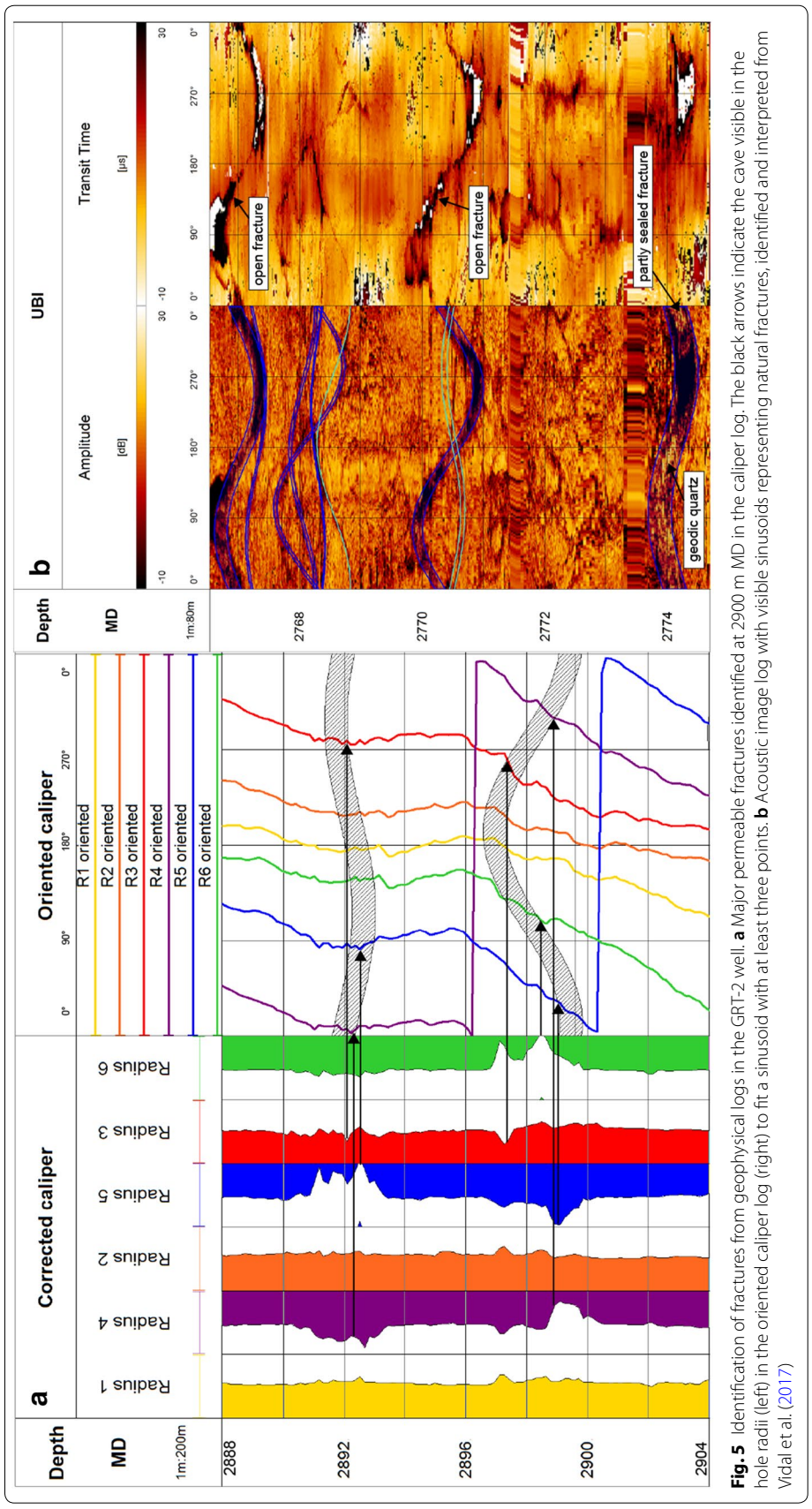

Fig. 5 Identification of fractures from geophysical logs in the GRT-2 well. **a** Major permeable fractures identified at 2900 m MD in the caliper log. The black arrows indicate the cave visible in the hole radii (left) in the oriented caliper log (right) to fit a sinusoid with at least three points. **b** Acoustic image log with visible sinusoids representing natural fractures, identified and interpreted from Vidal et al. (2017)

More precisely, negative temperature anomalies reveal permeable fractures that have been cooled during the drilling (Vidal et al. 2017), and positive anomalies are indicators of hot geothermal fluid circulation through a permeable fracture zone. The gamma ray (GR) log measures natural radioactivity (uranium, potassium, and thorium), and aids in interpretations of lithology and rock composition. In the altered crystalline basement, negative GR peaks in the lower positive domain can reflect quartz veins in illitized host rock (Genter et al. 2000). In the studied context, GR data are an indicator of hydrothermal alteration and thus provide information regarding paleopermeability. The porosity log (NPHI) represents measurements of the formation porosity by filling pores with hydrogen and can thus be highly influenced by clay and fluids. Porosity logs do not provide information on permeability but nevertheless provide a global signal for fractured zones to the extent that they are porous and contain clays and fluids. A density log (RHOB) is calculated from nuclear measurements emitted from a chemical source (Ce^{137} and Co^{60}). A negative peak in a density curve could be due to clays and thus reveal alteration associated with a fracture zone, whereas positive peaks are associated with high-density minerals or a change in lithology.

Resistivity log

A resistivity log is controlled by the electrical conductivity of the fluid contained in the rock porosity and by the electrical properties of the rock. Resistivity decreases in formations containing water and is even lower for conductive fluids that contain salts, such as brines. Similarly, resistivity is low for clay minerals, pyrite, and hematite, which are conductive minerals. Laterologs and focused resistivity arrays are common data acquisition tools for hydrocarbon wells carried out in sedimentary formations to find caprock or permeable zones containing oil or gas and to evaluate hydrocarbon saturation (Serra 1984). It is not possible to use the same petrophysical parameters to directly interpret laterolog resistivity in granite environments, because the contributions of matrix and fracture conductivities can vary by several orders of magnitudes among unaltered and altered granite zones and areas with different clay contents and fracture densities, whether or not sealed. Resistivity was measured with five electrode configurations, yielding five apparent resistivity values (RLA1–5) (Schlumberger 2018). These configurations are sensitive to different distances beyond the borehole wall. The shallowest resistivity (RLA1) reflects the average resistivity mainly of the borehole mud, and the deepest resistivity (RLA5) reflects the average resistivity of the formation. Some positive peaks in the GR curve can be directly linked to low resistivity values, such as at 2560 m MD [2220 m true vertical depth (TVD)] and 2830 m MD (2433 m TVD) (Fig. 7), and thus reflect clay properties.

To convert apparent resistivity into "true" formation resistivity, borehole caliper data, mud conductivity data, data from several electrode configurations (Schlumberger 2018), and other parameters have to be combined through an inversion procedure. Strictly speaking, petrophysical relationships should be applied to the inverted resistivity. Nevertheless, apparent resistivity behavior reflects an average of the formation properties except in places with sharp geometrical variations, such as those close to large fractures (Fig. 2, curves RLA1–5). In the presented work, only trends in the apparent resistivity

are compared with the other logs and models. See the detailed discussion later in this paper.

Results

Mineralogical log

The alteration minerals' distribution in the GRT-2 granitic section (2490–3196 m MD, 2165–2707 m TVD) is characterized by secondary geodic quartz that is well expressed from the top of the granite at 2490 m MD down to 2878 m MD and particularly in two zones at 2950 m MD (2527 m TVD) and 3052 m MD (2604 m TVD) (Fig. 2). Anhydrite precipitation is visible at the top of the basement to 2653 m MD (2292 m TVD) and from 2737 to 2875 m MD (2358–2469 m TVD) but is not visible in the deepest part of the well. Chlorite is ubiquitous in the GRT-2 borehole but is more concentrated in three zones: 2590–2734 m MD (2243–2356 m TVD), 2872–2935 m MD (2466–2515 m TVD), and 3073–3196 m MD (2620–2707 m TVD). The first and second chlorite zones contain relics of primary biotite that are partially chloritized, precisely corresponding to the HMOD facies, and are thus correlated with hydrothermal alteration. The third chlorite zone contains chloritized biotite that is clearly correlated with the GRAN facies, reflecting propylitic alteration. The illite content is very high at the top of the granitic basement and decreases down to the top of the unaltered granite (3060 m MD, 2610 m TVD), wherein there is no significant trace of illitic material in the cuttings. The oxidation is important in the top of the granitic basement, defining the RED facies unit, but decreases down to 2986 m MD (2955 m TVD). Calcite was measured in high quantities, with especially high values of 40% at 3052 m MD (2604 m TVD), 20% at 3000 m MD (2565 m TVD), and approximately 10% at 2570 and 3052 m MD (2228 and 2604 m TVD) (Fig. 2).

The secondary mineralogy of the GRT-1 well is characterized by globally less chlorite and more hematite than that of the GRT-2 well (Fig. 3). The alteration grade is also globally higher in the GRT-1 well than in the GRT-2 well; in fact, in the GRT-1 well, the alteration grade HEXT is observed from 2325 to 2350 m MD (2310–2335 m TVD), as evidenced by large amounts of illite and anhydrite. Secondary geodic quartz is only observed in one major fracture zone from 2357 to 2365 m MD (2341–2349 m TVD) and in one minor zone at 2325 m MD (2310 m TVD).

The granitic propylitic basement (GRAN) observed in the GRT-2 well corresponds to a massive and unaltered crystalline rock mass in the deepest part, down to 3196 m MD (Fig. 2). Above, hydrothermal alteration and a fracture system are highly developed. Fourteen facies zones grouped in three major thicker crystalline units were identified. At the top of the granitic basement, the first unit consists of reddish granite RED from 2479 to 2533 m MD (2155–2198 m TVD) and is characterized by a large amount of hematite and illitic phases. From 2533 to 3060 m MD (2198–2610 m TVD), the second unit is a large fractured zone that contains alteration minerals, such as illitic minerals, geodic quartz, and anhydrite. Four major fracture zones interpreted as quartz veins were delimited, ranging from 3 to 20 m in apparent thickness (at 2533, 2770, 2950, and 3052 m MD, i.e., 2198, 2885, 2527, and 2604 m TVD). These quartz veins contain large amounts of geodic quartz as well as calcite, and are strongly supported by local sharp temperature anomalies, negative GR anomalies, positive neutron porosity anomalies, and occasional

low bulk density peaks. Three alteration grades were also observed in the second unit: HLOW, HMOD, and HHIG. The third unit, in the deepest part of the well from 3060 to 3196 m MD (2610–2707 m TVD), consists of a GRAN zone and is characterized by very little hydrothermal alteration and a large amount of chlorite, reflecting the primary pervasive alteration of biotite. The boundary between the fracture zone unit and the deep unaltered granite unit in GRT-2 is characterized by a major permeable quartz zone (Fig. 2, 3052 m MD).

The granitic section in the GRT-1 well (2213–2582 m MD, 2200–2565 m TVD) is composed of oxidized propylitic granite (GRAN_OX) in the deepest part (2516–2582 m MD; 2500–2565 m TVD) and HLOW granite from 2409 to 2516 m MD (2393–2500 m TVD), which is the lowest alteration grade found in the GRT-1 granite (Fig. 3). Above, as in the GRT-2 well, a hydrothermally altered and fractured zone comprises four distinct facies zones. At the top of the granitic basement, the reddish granite extends from 2214 to 2274 m MD (2200–2260 m TVD) and contains a large amount of hematite. From 2274 to 2330 m MD (2260–2315 m TVD), a moderate illitic mineral content and sparse geodic quartz define the HHIG facies. A large fracture zone extends from 2330 to 2406 m MD (2315–2390 m TVD) and contains two major quartz veins with geodic quartz from 2366 to 2368 m MD (2350–2352 m TVD) and at 2327 m MD (2312 m TVD). The major quartz vein at 2366 m MD is strongly supported by a negative temperature anomaly, high mud losses, low GR anomaly, high porosity, and low density (Fig. 6). Surrounding the quartz veins, the HEXT facies are observed from 2330 to 2348 m MD (2315–2333 m TVD), and is characterized by large amounts of anhydrite, illitic minerals, and geodic quartz. From 2348 to 2409 m MD (2333–2393 m TVD), the HHIG facies are characterized by the presence of a large amount of chlorite, small amount of illite, and no geodic quartz.

Structural log

Fracture picking

Structural analysis has already been performed for most of the GRT-1 and GRT-2 wells but is lacking for the deepest part of the GRT-2 well (Vidal et al. 2017). However, new oriented caliper logs have been collected in some sections of the GRT-2 well where the structural analysis was not carried out (Fig. 6). We then focused on a structural fracture analysis of the GRT-2 well based on comparing only the acoustic image and oriented caliper logs. Four zones were studied. In the two first zones located at 2531 and at 2740 m MD (2196, 2360 m TVD) (Table 2), caliper results can be compared with UBI observations (Fig. 6). In zones 1 and 2, 26 fractures were observed in the caliper data, whereas 81 were found in the acoustic images (Fig. 6). Two major natural fractures were observed in zone 3, at 2895 m MD (2482 m TVD) with a dip direction of N117°E and a dip of 84° and at 2897 m MD (2486 m TVD) with a dip direction of N302°E and a dip of 70° (Fig. 5). Thus, from this analysis, the corrected caliper data enabled us to identify approximately 34% of the pre-existing fractures identified with the acoustic image log (Table 2). Two sets of fractures dipping towards ca. N50°E in zone 3 and ca. N80°E in zone 4 (with an accuracy of approximately 10°) were identified in the caliper data (Fig. 6).

The fracture picking process was applied to the caliper logs of the two deepest zones in GRT-2, where acoustic image logs were not available (Fig. 6). Zone 3, between 2880 and 2920 m MD (2472–2504 m TVD), and zone 4, between 2920 and 2960 m MD

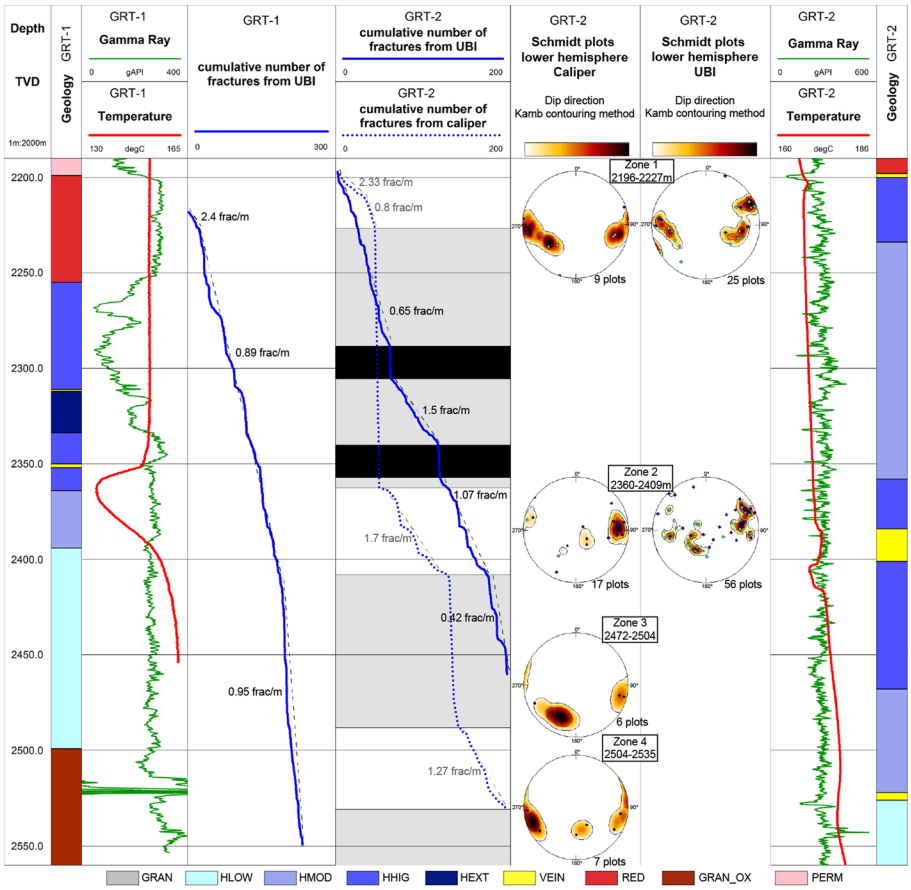

Fig. 6 Wells GRT-1 and GRT-2 with geology, temperature, and gamma ray data at the same depth. The cumulative number of fractures is from acoustic images for both wells and from the caliper data for the GRT-2 well. The fracture analysis was performed using stereographic diagrams, specifically, Schmidt lower hemisphere plots realized with the Kamb method; 2 specifies the initial contouring interval and 3 specifies the number of standard deviations that define the expected count for a uniform distribution. The stereographic diagrams were constructed based on both caliper and acoustic image log data for four major fracture zones in the granitic basement of the GRT-2 well. The black areas represent zones where UBI data was not acquired, and the gray areas represent zones where fractures from the caliper log were not computed. The UBI fracture datasets are from Vidal et al. (2016). The facies are as follows: GRAN: granite, HLOW: low hydrothermal alteration grade, HMOD: moderate alteration grade, HHIG: high alteration grade, HEXT: extreme hydrothermal alteration, VEIN: quartz vein, GRAN_OX: oxidized granite, RED: reddish granite, PERM: Permian sandstone

(2504–2535 m TVD), were selected for structural analysis. In zone 3, six major fractures with a mean dip direction of N52°E and a mean dip of 67° were found (Fig. 6). In zone 4, seven major fractures with a mean dip direction of N80°E and a mean dip of 87° were found (Fig. 6). The two fractures sets in zones 3 and 4 were also found in zones 1 and 2. Furthermore, zone 3 shows significant caves (borehole enlargements) located at approximately 2900 m MD (2488 m TVD), and zone 4, which is located around a quartz zone at 2950 m MD (2527 m TVD), features a negative thermal anomaly (Fig. 2). The fracture densities in zones 3 and 4 were slightly lower than those in zones 1 and 2.

Based on the lower density values, this structural analysis showed that fewer fractures were identified when only the corrected caliper data were used (Table 2). However, the

Table 2 Structural analysis of the GRT-2 granitic basement with the caliper

GRT-2	Corrected caliper			Acoustic image logs			Accuracy	
	Density (fract/m)	Dip direction		Density (fract/m)	Dip direction		Dip direction	dip
		Set 1	Set 2		Set 1	Set 2		
ZONE 1: 38 m (2196–2227 m TVD)	0.2	N274°E	N61°E	0.6	N263°E	N74°E	±11°	±5°
ZONE 2: 60 m (2360–2409 m TVD)	0.3	N272°E	N70°E	0.9	N265°E	N81°E	±9°	±13°
ZONE 3: 40 m (2472–2504 m TVD)	0.15	N52°E		*No data*			±10	±9°
ZONE 4: 40 m (2504–2535 m TVD)	0.17	N80°E		*No data*				

Comparison of the structural analyses and their accuracies as calculated from the caliper and acoustic image logs (zones 1 and 2). Structural analysis from caliper data only (zones 3 and 4)

two dominant directional fractures sets (east and west) were observed by the caliper and UBI methods.

Despite the low density of fractures identified with the corrected caliper data, the major fractures and their structural information for handling the well production were determined. This caliper correction approach enables us to obtain geometrical information from an inclined well and involves lower costs and risks than the collection of acoustic image logs.

Fracture density

The fracture densities in the GRT-2 well were compared using the cumulative fracture densities calculated from the acoustic image logs by Vidal et al. (2016) and those from the previously corrected caliper log (Fig. 6). The cumulative fracture density was calculated from the caliper for separated sections in the open-hole section, and the chosen delimitations are inflection points. Moreover, because the sections chosen for this study are not the same as those chosen in Vidal et al. (2016), they cannot be compared. To compare the caliper and UBI cumulative fracture densities for the GRT-2 well, even though the fractures were not sampled throughout the entire open-hole section from the caliper data, the cumulative fracture density calculated with the caliper log was calibrated with the total fracture number observed in the acoustic image log in the GRT-2 well. We observe that the cumulative fracture density from the caliper in GRT-2 seems to follow the same trend as the cumulative fracture density calculated from the acoustic images.

Electrical logs

Petrophysical observations

The following discussion is based on the apparent resistivity curve RLA5. As explained in "Resistivity log" section in this work, we did not invert resistivity logs to correct for borehole and mud effects; we used RLA5, as this measurement corresponds to the greatest depth in the surrounding formation and is surely the most representative of the true resistivity of the formation. The other resistivity measurements, RLA1–4, are also shown in Fig. 2. Although RLA1–4 represent the resistivity

closer to the borehole, they have a better vertical resolution than RLA5; thus, we show them in the figure for reference. Using apparent resistivity implies that geometrical structures, such as a dipping plane of constant resistivity crossing the well, are not interpreted as 2D/3D structures but as zones where the equivalent homogeneous resistivity varies (i.e., a 1D approach). This neglect of geometrical effects is valid far from contacts if the bedding thickness is larger than the sensitive zone of the electrodes' configuration. Furthermore, this technique is qualitatively valid as long as the geometrical effect does not dominate the electrical response or is almost constant in the studied interval. In the latter case, the logarithm of apparent resistivity is only shifted by a constant value from the true formation resistivity. Finally, note that the apparent resistivity curves show a smaller resistivity range than the true resistivity curves. For all these reasons, we limit our interpretations regarding the trends in the average resistivity data. Inversion of the apparent resistivity curve to true formation resistivity is outside the scope of the data presented in this article. This work is supported by a constant drilling diameter in the studied depth interval.

Petrophysical interpretations from the RLA5 apparent resistivity curve behavior and values are made in terms of alteration facies. Indeed, the hydrothermal alteration grades and resistivity seem to be clearly correlated. At the first order, the four permeable quartz veins observed in the GRT-2 well from cuttings yield resistivity responses between 0.2 and 60 ohm m, which clearly stand out on the electrical log. In terms of facies, the GRAN facies shows a resistivity response of approximately 3000 ohm m, the HMOD grade shows a resistivity response of approximately 400 ohm m, and the HHIG grade shows a resistivity response of approximately 60 ohm m (Fig. 2). The facies transitions are clearly visible in the resistivity curves, such as at 2740 and 2875 m MD between the HMOD and HHIG grades (Fig. 2, RLA5). The resistivity log trend is well correlated with the chlorite classes described in "Resistivity log" section, which were scaled from class one (smaller amount) to class three (larger amount) according to the relative amount of chlorite observed in the cuttings. The chlorite class three corresponds to high resistivity values between 200 and 20,000 ohm m (between 2600 and 2750 m MD for instance), whereas chlorite class one corresponds to lower resistivity values between 20 and 200 ohm m (Fig. 2).

Synthetic resistivity

A synthetic resistivity log based on observed physical measurements collected in the well was recalculated to study the contribution of electrolytic conductivity in pores (containing brine) and surface conduction (characterized by the CEC value) due to clay content. The resistivity formulas used are derived from the classic Archie (1942) and Waxman and Smits models (1968). More recent and complex models for computing the electrical conductivities of clay rocks have been published (Comparon 2005). From this overview, models based on different effective media (De Lima and Sharma 1990), varying in terms of the pore geometries, petrophysics, and surface properties of particles, are of high interest. The electrical conductivity is the inverse of the resistivity $\sigma = 1/\text{Res}$ (in S/m) and can be calculated as follows:

$$\sigma = \frac{\sigma_f}{F} + \frac{BQ_V}{F} \tag{1}$$

$$F = \emptyset^{-m} \quad \text{with } m = 2.2 \tag{2}$$

$$B = B_0 * \left[1 - 0.6 * \exp\left(-\frac{\sigma_f}{0.013}\right)\right] \tag{3}$$

$$Qv = \rho_g * \left(\frac{1-\phi}{\phi}\right) * \text{CEC}. \tag{4}$$

In Eq. (1), the first term, $\frac{\sigma_f}{F}$, corresponds to the Archie law that considers only the contribution of the water that fills the pore space (Archie 1942). σ_f is the conductivity of the geothermal water contained in the pore space in S/m, F is the formation factor, which depends on the rock porosity $\emptyset$, and m is the cementation factor (usually varying between 2 and 3), as shown in Eq. (2).

The second term, $\frac{BQ_V}{F}$, corresponds to the surface conduction introduced in the Waxman and Smits model that considers the clays contribution (Revil et al. 1998; Waxman and Smits 1968). B is the ionic mobility of the compensating ions. NaCl dominates the brine ionic species, and we used the ionic mobility of sodium by considering that the excess of charges is negative and that only Na compensates the charge movement due to the flow of electric current. Q_V depends on rock porosity $\emptyset$, grain density ρ_g, and the CEC value in meq/100 g (see Eq. 4).

CEC measurements were performed on several cutting samples in which the clay contents were characterized by XRD and were performed on samples from several fracture zones and from the several granitic facies (Fig. 2). In the presence of clays, the CEC values influence the resistivity through Eq. (4). In total, 8 CEC laboratory analyses were conducted for the granitic basement of the GRT-2 well (Bouchet et al. 2017). The CEC values were found to be inversely proportional to the chlorite quantity. An extrapolated *CEC* synthetic log was calculated from 2500 to 2900 m MD based on the chlorite classes (Fig. 2), with values of 4.3 meq/100 g for class one, 3.5 meq/100 g for class two, and 1.9 meq/100 g for class three. Indeed, the *CEC* values vary between the mineralogical chlorite endmember and the illite endmember (corresponding to higher and lower CEC values, respectively).

The ionic mobility is affected by temperature, and consequently, the conductivity of the pore water is also sensitive to temperature. A conductivity increase of approximately 2.3%/°C is widely accepted in the literature. At 1 bar, this empirical pattern is reliable up to temperatures reaching 85 °C. We used the variation trend from Eq. (5) (Revil et al. 1998) to calculate the temperature effect at higher temperatures, because the brine remains liquid under the pressure conditions in the Rittershoffen well:

$$B0(T) \approx B(25\ ^\circ\text{C}) * \left[1 + \upsilon_f * (T - 25)\right] \quad \text{and } \sigma_f(T) \approx \sigma_f(25\ ^\circ\text{C}) * \left[1 + \upsilon_f * (T - 25)\right], \tag{5}$$

with $\upsilon_f \approx 0.023\ ^\circ\text{C}^{-1}$ and $B(25\ ^\circ\text{C}) = 5.19\ *\ 10^{-8}$

In the investigated depth section at Rittershoffen, the temperature ranges between 160 and 180 °C (Fig. 2). A temperature variation of 20 °C means a resistivity variation of 40% based on Eq. (5). This variation is moderate compared to the observed range in resistivity values of 0.2 to 10,000 ohm m (Fig. 7), and temperature is not the main driver of the

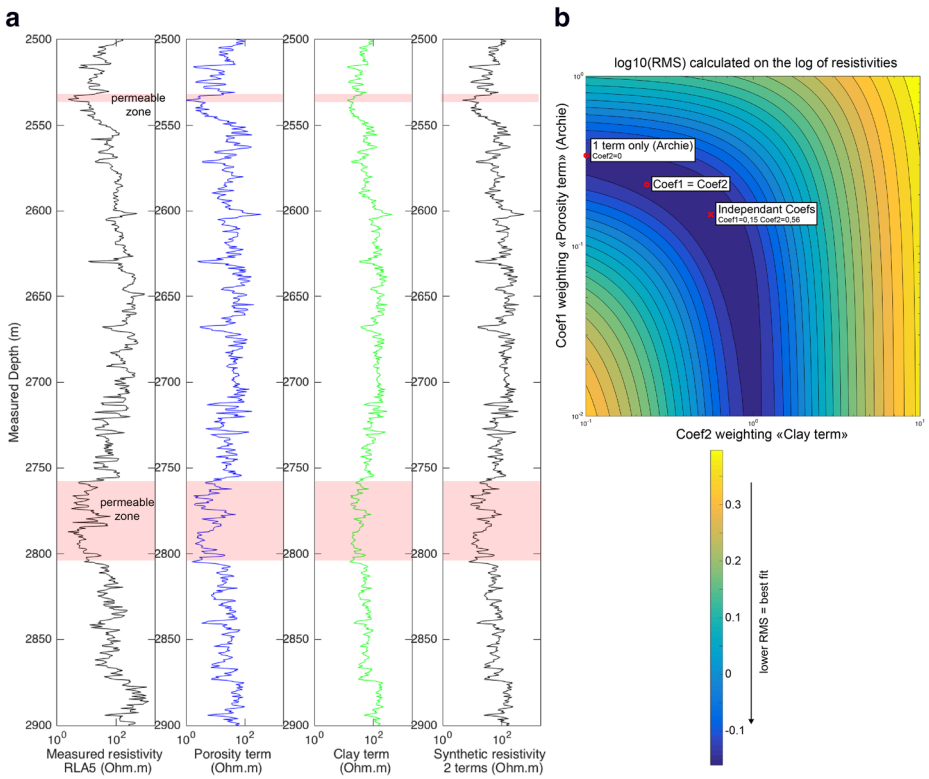

Fig. 7 Comparison of the measured and calculated electrical logs. **a** From left to right: measured apparent resistivity, contribution of the porosity to the calculated resistivity (Archie term), contribution of the clays to the calculated resistivity, and recalculated synthetic resistivity. Red zones indicate permeable fracture zones. **b** Consequences of the independent weighting of the Archie term (*y*-axis) and the clay term (*x*-axis) for the fit of the resistivity model [RMS in log(ohm m)]. The optimal solution includes two independent coefficients (red cross) and produces the lowest RMS value (dark blue)

resistivity changes observed here. The density log (RHOZ) is employed as grain density ρ_g, and the mean density value measured in the GRT-2 well is 2650 kg/m^3 (Fig. 2). The cementation factor m is taken to be 2.2 (Belghoul 2007). The rock porosity $\emptyset$ is taken from the neutron porosity log (NPHI), and it, therefore, varies with depth up to 17%. The fluid conductivity measured at 25 °C is 13.7 S/m in the GRT-1 well, and the fluid salinity is approximately 100 g/L NaCl equivalent in both the GRT-1 and GRT-2 wells (Sanjuan et al. 2016). Thus, based on those values and an extrapolation of a temperature correction derived from Eq. (5), the fluid conductivity is fixed at 30 S/m.

Using the model in Eq. (1), we calculated a synthetic resistivity log by weighting the two terms through the coefficients coef1 and coef2 defined in Eq. (6):

$$\sigma = \text{coef}_1 * \frac{\sigma_f}{F} + \text{coef}_2 * \frac{BQ_V}{F}. \tag{6}$$

Coef1 controls the contribution of NPHI through the Archie law term (Fig. 7a, porosity term). Coef2 controls the weight of the clay contribution based on the extrapolated CEC log and RHOZ (Fig. 7a, clay term). Synthetic logs were also adjusted using coef1 only (i.e., coef2 = 0) to fit the measured resistivity log but could not reach a fit that was as good as that with both terms. We considered the optimization process using

the resistivity or the logarithm of resistivity, various depth intervals (>50 m), and the RLA3–5 data, which provided almost the same results. Hence, only results using RLA5 are presented here. Figure 7a shows the logs from 2500 to 2900 m MD used in the calculation, which are, from left to right, the RLA5 data, the porosity term (through the Archie law), the clay term, and finally the sum of these two terms based on Eq. (6), which is the synthetic log that best fits the RLA5 data. A satisfactory model means minimizing the root mean square (RMS) calculated according to Eq. (7) (Fig. 7b):

$$\mathrm{RMS} = \sqrt{\sum \left(\log\left(\mathrm{Rho}_{\mathrm{calc}}\right) - \log\left(\mathrm{Rho}_{\mathrm{meas}}\right)\right)^2 / N}, \tag{7}$$

where $\mathrm{Rho}_{\mathrm{calc}}$ is the synthetic resistivity, $\mathrm{Rho}_{\mathrm{meas}}$ is the measured resistivity, and N is the number of resistivity values.

Optimization is illustrated in the cross-plot in Fig. 7b, which compares the best fits obtained with one term and with two terms. The synthetic curve modeled with two terms has a lower (better) RMS value (0.69 with independent coefficients and 0.71 log(ohm m) with coef1 = coef2, which correspond to a factor of 2 = exp(0.7) between synthetic and field resistivity values) than the synthetic curve calculated with only the porosity term [1.3 log(ohm m), which corresponds to a factor of 4 between synthetic and field resistivity values]. Thus, a higher correlation coefficient and a lower RMS value are achieved. The resulting correlation coefficient (on the logarithm of resistivity) obtained for the synthetic resistivity calculated with two coefficients is 85%, compared to 82% for coef1 = coef2 and 79% when using only the porosity term (Archie law). Note that optimization with two coefficients decreases the relative weight of the Archie term (related to porosity and water conductivity) and increases the relative weight of the term related to the clay contribution (the respective weights are 0.15 and 0.50). Therefore, when using only the clay term, good fit results are also obtained (Fig. 7b).

The permeable fractures were found to correspond to the lowest resistivity peaks, which were controlled by the brine conductivity through the "porosity term" contribution to the resistivity (Fig. 7a). To better explain the resistivity curve trend in other locations, the clay contribution has to be considered. We will pursue this work on inverted resistivity by combining the RLA1–5 data in other wells in similar contexts and by considering petrophysical measurements on samples.

Discussion

Correlation between well and mud log data

The various datasets enabled characterization of the hydrothermal alteration grades and identification of permeable fracture zones in the granite. The unaltered granite zone is characterized by a steady GR value of approximately 260 gAPI, a neutron porosity of approximately 5%, a steady bulk density value of approximately 2.65 g/cm^3, an ROP value of approximately 7 m/h, a high resistivity value of approximately 3000 ohm m, and a linear temperature profile (Fig. 2). However, the altered granite (HMOD, HHIG, and HEXT) is characterized by variable GR values of approximately 320 gAPI, variable ROP values ranging from 4 to 10 m/h, low resistivity values between 60 and 500 ohm m, and calcite contents higher than 5%. Furthermore, alteration minerals such as illite are abundant, and euhedral quartz is regularly present (Figs. 2, 8). Permeable fracture zones are

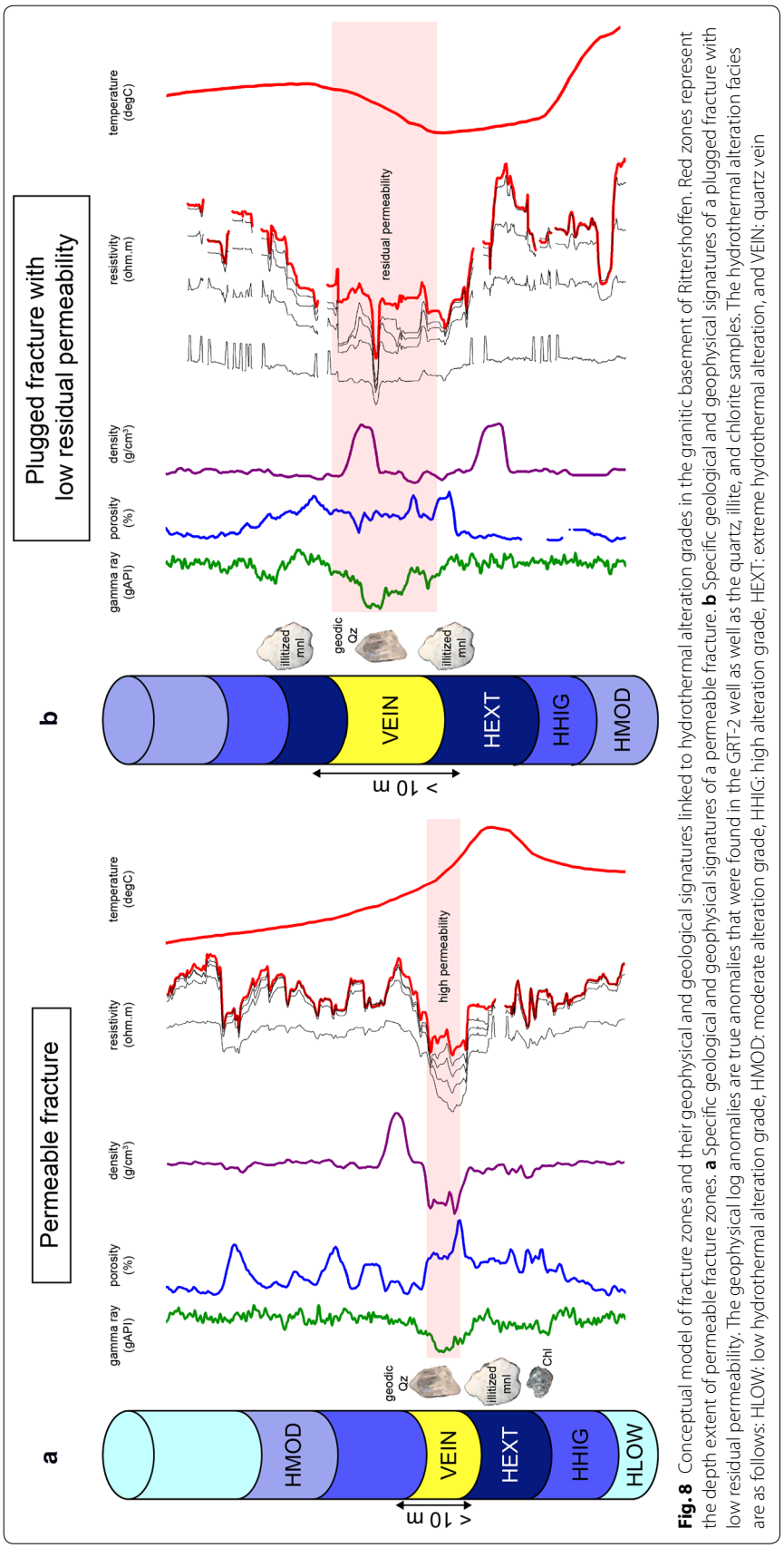

Fig. 8 Conceptual model of fracture zones and their geophysical and geological signatures linked to hydrothermal alteration grades in the granitic basement of Rittershoffen. Red zones represent the depth extent of permeable fracture zones. **a** Specific geological and geophysical signatures of a permeable fracture. **b** Specific geological and geophysical signatures of a plugged fracture with low residual permeability. The geophysical log anomalies are true anomalies that were found in the GRT-2 well as well as the quartz, illite, and chlorite samples. The hydrothermal alteration facies are as follows: HLOW: low hydrothermal alteration grade, HMOD: moderate alteration grade, HHIG: high alteration grade, HEXT: extreme hydrothermal alteration, and VEIN: quartz vein

associated with the VEIN facies. An abundance of euhedral quartz is the indicator of past or present hydrothermal circulation. Moreover, temperature anomalies were found to be systematically correlated with the quartz zones (Figs. 2, 6). For example, from 2770 to 2791 m MD in GRT-2 (Fig. 2, 2385–2400 m MD), the fracture zone is characterized by a large amount of illite and increasing mud losses from 10 to 13 m^3/h. This quartz zone is also associated with temperature anomalies, shifting from a positive anomaly at 2772 m MD to a negative anomaly at 2794 m MD (Fig. 2).

Fracture zone detected from well and mud log data

From cutting observations, four quartz zones were found in the GRT-2 well at 2530, 2770–2790, 2950, and 3052 m MD (Fig. 2), and two were found in the GRT-1 well at 2326 m and 2365 m MD (2311–2349 m TVD) (Fig. 3). These permeable fracture zones were previously observed by Vidal et al. (2016) in UBI logs. They also match the occurrence of small crystallites of illite and illite/smectite-mixed layers (Vidal et al. 2018). To complete the structural information on fractures, this study attempted to identify fractures in the caliper log in the deepest part of the GRT-2 well (where no acoustic images had been acquired). The resistivity signature was found to correlate with the occurrence of quartz veins in the GRT-2 well (Fig. 2). For example, at 3052 m MD, the quartz vein extent corresponds to the resistivity anomaly extent in terms of depth (Figs. 2, 7). This zone also exhibits intense argillization and a high calcite content, which suggest past massive hydrothermal alteration associated with fracture filling. This fracture zone is an interface between the altered and fractured granite and the unaltered granite (Fig. 2). The fractured and altered granite could represent the hanging wall of a fault, and the unaltered granite could represent the foot wall. Thus, the interface between them could be interpreted as the local normal fault accommodating the majority of displacement in Rittershoffen, which is the initial geothermal target. This observation is similar to the occurrence of a major permeable fracture zone observed in well GRT-1 from 2326 m to 2365 m MD (2311–2349 m TVD) (Fig. 3). Due to the geological contrast between the two distinct sections, this interface is assumed to be the trace of a local normal fault with a high degree of natural permeability. A new interpretation of the seismic data with consideration of the results at the well scale could help support this idea.

Resistivity signature of permeable fracture zones

The several types of hydrothermal alteration observed in the cuttings are clearly correlated with the resistivity signature (Fig. 2), and both porosity and clay content/type control the resistivity values, with the clay term dominating (Fig. 7). In addition, the responses of fracture zones in the granitic basement in the geophysical logs can also be very different in terms of depth extent and amplitude (Figs. 2, 8). In GRT-2, temperature anomalies are consistently linked to the occurrence of permeable fracture zones, but they can extend spatially from 3 to 24 m in depth (MD) and vary from $+2$ to -3 °C (Baujard et al. 2017a; Vidal et al. 2017). In addition, there is an evident correlation among the lengths of a temperature anomaly, the fractured zone sampled with the caliper and the resistivity anomaly zone in the electrical logs. For example, in the fracture zone at 2530 m MD, the length of the temperature anomaly, the length of the zone with an enlarged hole diameter, and the length of the resistivity

anomaly zone are all approximately 3 m (Fig. 8). The fracture zones at 2770, 2790, and 3052 m MD exhibit temperature anomaly lengths from 14 to 24 m, which are similar to the lengths of the corresponding resistivity and hole diameter anomalies. For the fracture zone at 2950 m MD, the temperature anomaly is very smooth, and the 1 °C temperature variation extends for more than 50 m in depth; thus, this anomaly is difficult to associate with the resistivity anomaly extent.

Hierarchy of permeable fracture zones

A hierarchy of the major permeable fractures in terms of contribution to well productivity was established based on secondary mineralogy, structural information, and geophysical log responses (temperature and resistivity) in the GRT-2 well. The permeable fracture zone at 2770–2790 m MD (2385–2400 m TVD) is assumed to offer the greatest contribution to well productivity, because it exhibits a considerable temperature anomaly (Baujard et al. 2017a).

The uppermost permeable fracture at the sediment–basement transition at 2535 m MD (2200 m TVD) presents localized and sharp geophysical anomalies that extend over less than 10 m in depth. A positive temperature anomaly in this area could indicate a hot geothermal outflow through open fractures (Vidal et al. 2017). The GR anomaly at 2535 m MD indicates spatially limited alteration zones around the open fractures. Moreover, chlorite is still observed at this depth, indicating that illitization has not yet plugged the zone. Other fracture zones, such as at 3052 m MD (2604 m TVD), present very low GR peaks, indicating that these zones have experienced more hydrothermal circulation than for the uppermost one.

The deepest fracture at the transition between the altered and fractured granite and the unaltered granite at 3052 m MD presents broad extended geophysical anomalies larger than 10 m. The highest porosities and lowest densities are located at the extremities of the GR peak, and this zone could be interpreted as an altered and porous zone around the open fracture. The large negative GR anomaly could indicate that open fractures in the core of the zone are now plugged by small crystallites of illite. Chlorite is no longer observed, and calcite is present in high proportions (40%), as a result of long-term hydrothermal circulation leading to chlorite alteration and precipitation of minerals such as illite and calcite (Sausse et al. 1998) (Fig. 2). Thus, the residual permeability of the fracture zone has likely been reduced by secondary mineralization. The negative temperature anomaly could be the effect of the remnant cooling of the porous and altered zone after mud circulation during drilling. The cooling of porous zones has also been observed in other geothermal wells (Barton et al. 1995; Bradford et al. 2013; Davatzes and Hickman 2005). In addition, the fracture zone at 2950 m MD (2527 m TVD) could also be one of the less contributive to the GRT-2 well productivity. In fact, its negative temperature anomaly has a relatively large depth extent, i.e., approximately 50 m, which could indicate a large porous and altered zone around the fracture core. The core of the fracture zone is located at precisely 2950 m MD based on the quartz VEIN facies, a negative GR peak, a higher porosity, and a lower density.

Conclusions

The compilation of various datasets for the GRT-2 geothermal production well has yielded a detailed petrographic log and new permeability estimates, and the geophysical logs can be used to perform structural analyses. In this study on the granitic basement, the major permeable fracture zones associated with high permeabilities were identified. The precision of the cuttings with depth was found to be sufficient to identify fracture cores based on quartz veins and altered and porous zones based on the small size of illite crystallites.

The caliper log was improved with geometrical corrections, which resulted in less accurate structural information on fracture zones than the analysis based on UBI data. However, this technique is promising for situations in which other geophysical logs cannot be performed. Furthermore, caliper data are cheaper to obtain and are effective for identifying significant fractures.

Petrophysical laws were applied to recalculate a synthetic resistivity log for the granitic basement, which showed a very good correlation with the measured resistivity log. The electrical resistivity model from the Rittershoffen case study will be applied to previously collected and new data sets from other granite-hosted geothermal sites, such as at Soultz and Illkirch. Unlike temperature anomalies, the resistivity signature of a fracture zone can provide an accurate, quantitative estimate of the permeability of the granite. At Rittershoffen, an interesting correlation was observed between the depth extents of the temperature and resistivity anomalies. The fractures that contribute most to the actual well productivity are associated with localized anomalies in the geophysical logs. These fractures are also characterized by positive temperature anomalies that are interpreted as hot-water outflows in the well. In contrast, fractures in the deepest part of GRT-2 seem to be plugged by small crystallites of illitic material and calcite due to past massive hydrothermal circulation. These fractures are characterized by broad anomalies in the geophysical logs. The fractures with low residual permeabilities are associated with negative temperature anomalies that are interpreted as cooling of the porous altered zone by mud circulation during drilling.

Abbreviations

CEC: cation exchange capacity (meq/100 g); EDS: energy-dispersive X-ray spectroscopy; EGS: enhanced geothermal system; GR: gamma ray (gAPI); GRAN: granite; GRAN_OX: oxidized granite; GRT-1: "Géothermie Rittershoffen 1", injection well; GRT-2: "Géothermie Rittershoffen 2", production well; HEXT: extreme hydrothermal alteration; HHIG: high hydrothermal alteration; HLOW: low hydrothermal alteration; HMOD: moderate hydrothermal alteration; MD: measured depth; NPHI: thermal neutron porosity (original ratio method) in selected lithology (m^3/m^3); PERM: permian sandstones; RED: reddish granite; RHOZ: standard-resolution formation density (g/cm^3); RLA1–5: apparent resistivity from computed focusing mode 1–5 (ohm m); RMS: root mean square; ROP: rate of penetration; SEM: scanning electron microscope; SsF: Soultz-sous-Forêts; THMC: thermo-hydro-mechanical-chemical; TVD: true vertical depth; UBI: ultrasonic borehole imager; URG: Upper Rhine Graben; VEIN: quartz vein; XRD: X-ray diffraction.

Authors' contributions

CG and AG worked on petrographical log (data analysis and interpretation). CG and JFG worked on electrical logs (data analysis and interpretation). All authors contribute to the conceptual model and final version of this article. All authors read and approved the final manuscript.

Author details

[1] ES Géothermie, 5 RUE de Lisbonne, 67300 Schiltigheim, France. [2] CNRS, UMR 7516 IPGS, University of Strasbourg, 5 Rue René Descartes, 67084 Strasbourg Cedex, France. [3] CNRS UMR 7285 IC2MP, HydrASA, University of Poitiers, Bat B8, Rue Albert Turpain, TSA51106, 86073 Poitiers Cedex 9, France.

Acknowledgements

This work is based on data from the ECOGI geothermal project at Rittershoffen, France. This work was undertaken and co-funded by ÉS-Géothermie in the framework of the EGS Alsace project, which is co-funded by ADEME, the ÉS group,

and EOST. This work was undertaken as a contribution to the Ph.D. thesis of Carole Glaas and was co-funded by ANRT (French Research and Technology Agency) and ÉS-Géothermie. The authors want to acknowledge Dr. Philippe Leroy for his help with calculating the clay contribution to electrical conductivity in our model. The authors appreciate the helpful and constructive remarks of Dr. Carola Meller and two anonymous reviewers, which seriously improved the manuscript.

Competing interests
The authors declare that they have no competing interests.

Availability of data and materials
Data belong to ECOGI. Please contact ES-Géothermie for data requests at geothermie@es.fr.

Publisher's Note

Received: 20 March 2018 Accepted: 10 July 2018
Published online: 23 July 2018

References

Archie GE. The electrical resistivity log as an aid in determining some reservoir characteristics. Trans AIME. 1942;146:54–62. https://doi.org/10.2118/942054-G.

Baillieux P, Schill E, Abdelfettah Y, Dezayes C. Possible natural fluid pathways from gravity pseudo-tomography in the geothermal fields of Northern Alsace (Upper Rhine Graben). Geotherm Energy. 2014;2:16. https://doi.org/10.1186/s40517-014-0016-y.

Barton CA, Zoback MD, Moos D. Fluid flow along potentially active faults in crystalline rock. Geology. 1995; 23:683–6. https://doi.org/10.1130/0091-7613(1995)023<0683:FFAPAF>2.3.CO;2.

Bauer JF, Meier S, Philipp SL. Architecture, fracture system, mechanical properties and permeability structure of a fault zone in Lower Triassic sandstone, Upper Rhine Graben. Tectonophysics. 2015. https://doi.org/10.1016/j.tecto.2015.02.014.

Baujard C, Hehn R, Genter A, Teza D, Baumgartner J, Guinot F, Martin A, Steinlechner S. Rate of penetration of geothermal wells: a key challenge in hard rocks. In: Workshop on geothermal reservoir engineering. Stanford University, USA; 2017b.

Baujard C, Genter A, Dalmais E, Maurer V, Hehn R, Rosillette R, Vidal J, Schmittbuhl J. Hydrothermal characterization of wells GRT-1 and GRT-2 in Rittershoffen, France: implications on the understanding of natural flow systems in the Rhine Graben. Geothermics. 2017;65:255–68. https://doi.org/10.1016/j.geothermics.2016.11.001.

Belghoul A. Caractérisation pétrophysique et hydrodynamique du socle cristallin (PhD). France: Montpellier II; 2007.

Bouchet A, Morin C, Parneix JC. Mesure de la C.E.C. de onze échantillons. (Internal Report ESG No. ERM 17 082 AB 108). ERM, Poitiers; 2017.

Bradford J, McLennan J, Moore J, Glasby D, Waters D, Kruwell R, Bailey A, Rickard W, Bloomfield K, King D. Recent developments at the raft river geothermal field. In: Presented at the 38th workshop on geothermal reservoir engineering. Stanford University, California, USA; 2013.

Cocherie A, Guerrot C, Fanning CM, Genter A. Datation U-Pb des deux faciès du granite de Soultz (Fossé rhénan, France). Comptes Rendus Geosci. 2004;336:775–87. https://doi.org/10.1016/j.crte.2004.01.009.

Comparon L. Experimental study of the electrical and dielectric properties of consolidated clayey materials (PhD). France: Institut de Physique du Globe de Paris; 2005.

Davatzes NC, Hickman SH. Controls on fault-hosted fluid flow; Preliminary results from the Coso Geothermal Field, CA. In: Presented at the geothermal resources council transactions, geothermal resources council, Davis, California. 2005. p 343–8.

De Lima O, Sharma M. A grain conductivity approach to shaly sandstones. Geophysics. 1990;55:1347–56. https://doi.org/10.1190/1.1442782.

Dezayes C, Genter A, Valley B. Structure of the low permeable naturally fractured geothermal reservoir at Soultz. Comptes R Geosci. 2010;342:517–30. https://doi.org/10.1016/j.crte.2009.10.002.

Faulkner DR, Jackson CAL, Lunn RJ, Schlische RW, Shipton ZK, Wibberley CAJ, Withjack MO. A review of recent developments concerning the structure, mechanics and fluid flow properties of fault zones. J Struct Geol. 2010;32:1557–75. https://doi.org/10.1016/j.jsg.2010.06.009.

Gailler L-S, Bouchot V, Martelet G, Thinon I, Coppo N, Baltassat J-M, Bourgeois B. Contribution of multi-method geophysics to the understanding of a high-temperature geothermal province: the Bouillante area (Guadeloupe, Lesser Antilles). J Volcanol Geotherm Res. 2014;275:34–50. https://doi.org/10.1016/j.jvolgeores.2014.02.002.

Genter A. Géothermie roches chaudes sèches : le granite de Soultz-sous-Forêts (Bas-Rhin, France). Fracturation naturelle, altérations hydrothermales et interaction eau-roche (PhD). Université d'Orléans, France. 1989.

Genter A, Traineau H, Artignan D. Synthesis of geological and geophysical data of Soultz-sous-Forêts (France) (Open-File Report No. R39440). BRGM. 1997.

Genter A, Traineau H, Ledésert B, Bourgine B, Gentier S. Over 10 years of geological investigations within the HDR Soultz project, France. In: Presented at the world geothermal congress, Kyushu, Japan. 2000.

GeOrg Team. EU-Projekt GeORG-Geoportal [WWW Document]. 2017. http://www.geopotenziale.org/home?lang=3.

Griffiths L, Heap MJ, Wang F, Daval D, Gilg HA, Baud P, Schmittbuhl J, Genter A. Geothermal implications for fracture-filling hydrothermal precipitation. Geothermics. 2016;64:235–45. https://doi.org/10.1016/j.geothermics.2016.06.006.

Gudmundsson A, Fjeldskaar I, Brenner LS. Propagation pathways and fluid transport of hydrofractures in jointed and layered rocks in geothermal fields. J Volcanol Geotherm Res. 2002;116:257–78. https://doi.org/10.1016/S0377-0273(02)00225-1.

Hébert RL, Ledésert B, Bartier D, Dezayes C, Genter A, Grall C. The enhanced geothermal system of Soultz-sous-Forêts: a study of the relationships between fracture zones and calcite content. J Volcanol Geotherm Res. 2010;196:126–33. https://doi.org/10.1016/j.jvolgeores.2010.07.001.

Ishibashi M, Yoshida H, Sasao E, Yuguchi T. Long term behavior of hydrogeological structures associated with faulting: an example from the deep crystalline rock in the Mizunami URL, Central Japan. Eng Geol. 2016;208:114–27. https://doi.org/10.1016/j.enggeo.2016.04.026.

Jacquemont B. Etude des interactions eaux-roches dans le granite de Soultz-sous-Forêts. Quantification et modélisation des transferts de matière par les fluides (PhD). Université de Strasbourg, France. 2002.

Ledésert B, Dubois J, Genter A, Meunier A. Fractal analysis of fractures applied to Soultz-sous-Forets hot dry rock geothermal program. J Volcanol Geotherm Res. 1993;57:1–17. https://doi.org/10.1016/0377-0273(93)90028-P.

Ledésert B, Berger G, Meunier A, Genter A, Bouchet A. Diagenetic-type reactions related to hydrothermal alteration in the Soultz-sous-Forets Granite, France. Eur J Mineral. 1999;11:731–41.

Ledésert B, Hebert R, Genter A, Bartier D, Clauer N, Grall C. Fractures, hydrothermal alterations and permeability in the Soultz enhanced geothermal system. Comptes Rendus Geosci. 2010;342:607–15. https://doi.org/10.1016/j.crte.2009.09.011.

Meller C, Kohl T. The significance of hydrothermal alteration zones for the mechanical behavior of a geothermal reservoir. Geotherm Energy. 2014. https://doi.org/10.1186/s40517-014-0012-2.

Meller C, Ledésert B. Is there a link between mineralogy, petrophysics, and the hydraulic and seismic behaviors of the soultz-sous-forêts granite during stimulation? A review and reinterpretation of petro-hydromechanical data toward a better understanding of induced seismicity and fluid flow. J Geophys Res Solid Earth. 2017;122:9755–74. https://doi.org/10.1002/2017JB014648.

Meller C, Genter A, Kohl T. The application of a neural network to map clay zones in crystalline rock. Geophys J Int. 2014;196:837–49. https://doi.org/10.1093/gji/ggt423.

Moreno L, Neretnieks I. Fluid flow and solute transport in a network of channels. J Contam Hydrol. 1993;14:163–92. https://doi.org/10.1016/0169-7722(93)90023-L.

Revil A, Cathles LM III, Losh S, Nunn JA. Electrical conductivity in shaly sands with geophysical applications. J Geophys Res. 1998;103:23925–36. https://doi.org/10.1029/98JB02125.

Rotstein Y, Edel J-B, Gabriel G, Boulanger D, Schaming M, Munschy M. Insight into the structure of the Upper Rhine Graben and its basement from a new compilation of Bouguer Gravity. Tectonophysics. 2006;425:55–70. https://doi.org/10.1016/j.tecto.2006.07.002.

Sanjuan B, Millot R, Innocent C, Dezayes C, Scheiber J, Brach M. Major geochemical characteristics of geothermal brines from the Upper Rhine Graben granitic basement with constraints on temperature and circulation. Chem Geol. 2016;428:27–47. https://doi.org/10.1016/j.chemgeo.2016.02.021.

Sausse J, Genter A. Types of permeable fractures in granite. Geol Soc Lond Spec Publ. 2005;240:1–14. https://doi.org/10.1144/GSL.SP.2005.240.01.01.

Sausse J, Genter A, Leroy JL, Lespinasse M. Description et quantification des alterations filoniennes; paleoecoulements fluides dans le granite de Soultz-sous-forets (Bas-Rhin, France). Bull Société Géologique Fr. 1998;169:655–64.

Sausse J, Fourar M, Genter A. Permeability and alteration within the Soultz granite inferred from geophysical and flow log analysis. Geothermics. 2006;35:544–60.

Sausse J, Dezayes C, Dorbath L, Genter A, Place J. 3D model of fracture zones at Soultz-sous-Forêts based on geological data, image logs, induced microseismicity and vertical seismic profiles. Comptes Rendus Geosci. 2010;342:531–45. https://doi.org/10.1016/j.crte.2010.01.011.

Schill E, Genter A, Cuenot N, Kohl T. Hydraulic performance history at the Soultz EGS reservoirs from stimulation and long-term circulation tests. Geothermics. 2017;70:110–24. https://doi.org/10.1016/j.geothermics.2017.06.003.

Schlumberger. HRLA High-Resolution Laterolog Array| Schlumberger [WWW Document]. Schlumberger. 2018. https://www.slb.com/services/characterization/petrophysics/wireline/legacy_services/high_res_array.aspx. Accessed 3 Dec 2018.

Serra O. Fundamentals of well-log interpretation. Elsevier ed. Pau: ELF Aquitaine; 1984.

Stober I, Bucher K. Hydraulic properties of the crystalline basement. Hydrogeol J. 2007;15:213–24. https://doi.org/10.1007/s10040-006-0094-4.

Stussi J-M, Cheilletz A, Royer J-J, Chèvremont P, Féraud G. The hidden monzogranite of Soultz-sous-Forêts (Rhine Graben, France). Mineralogy, petrology and genesis. Géologie Fr. 2002;1:45–64.

Traineau H, Genter A, Cautru JP, Fabriol H, Chevremont P. Petrography of the granite massif from drill cutting analysis and well log interpretation in the geothermal HDR borehole GPK1 (Soultz, Alsace, France). Geotherm Sci Technol. 1991;3:1–29.

Vidal J, Genter A. Overview of naturally permeable fractured reservoirs in the central and southern Upper Rhine Graben: insights from geothermal wells. Geothermics. 2018;74:57–73. https://doi.org/10.1016/j.geothermics.2018.02.003.

Vidal J, Genter A, Chopin F, Dalmais E. Natural fractures and permeability at the geothermal site Rittershoffen, France. In: Presented at the European geothermal congress, Strasbourg, France; 2016.

Vidal J, Genter A, Chopin F. Permeable fracture zones in the hard rocks of the geothermal reservoir at Rittershoffen, France. J Geophys Res Solid Earth. 2017;122:4864–87. https://doi.org/10.1002/2017JB014331.

Vidal J, Patrier P, Genter A, Beaufort D, Dezayes C, Glaas C, Lerouge C, Sanjuan B. Clay minerals related to the circulation of geothermal fluids in boreholes at Rittershoffen (Alsace, France). J Volcanol Geotherm Res. 2018;349:192–204. https://doi.org/10.1016/j.jvolgeores.2017.10.019.

Villemin T, Bergerat F. L'évolution structurale du fossé rhénan au cours du Cénozoïque: un bilan de la déformation et des effets thermiques de l'extension. Bull Soc Géol Fr. 1987;8:245–55.

Waxman MH, Smits LJ. Electrical conductivities in oil-bearing shaly sands. In: Presented at the 42nd annual fall meeting, journal of society of petroleum engineers. 1968. p 107–22.